LASER-PLASMA ION GENERATOR OF A WIDE RANGE OF ELEMENTS FOR A HEAVY-ION INJECTOR OF SYNCHROTRONS

© 2025 A. N. Balabaev, A. A. Vasilyev, T. V. Kulevoy, A. A. Losev, Yu. A. Satov, I. A. Khrisanov*, A. V. Shumshurov

National Research Center "Kurchatov Institute" Russia, Moscow

**e-mail: hrisanov@itep.ru*

Received July 21, 2024
Revised August 09, 2024
Accepted September 23, 2024

Abstract. The paper describes the results of the first experiments on generating ions from a number of chemical elements from light to heavy using a laser-plasma ion source, which is part of the heavy-ion injector of synchrotrons being developed at the Kurchatov Institute National Research Center. The source is based on the FOCUS CO2 laser system of pulse-periodic action and includes a vacuum target chamber with a drift space and a high-voltage system for extraction and formation of a beam of charged particles. The paper describes the device of the source and presents the characteristics of the laser radiation and generated ion beams of Al, Fe and Bi, which were obtained as a result of joint processing of the time-of-flight spectrum of particles from the plasma flow and the current characteristics of the extracted ion beam. The high efficiency of this source for obtaining intense ion beams from a wide range of elements and the possibility of their prompt replacement can be successfully used in synchrotron injectors for complex studies and testing of the electronic component base for radiation resistance.

DOI: 10.31857/S00328162250103e9

1. INTRODUCTION

The use of pulsed lasers in ion sources has significantly expanded the traditional areas of use of accelerated particle beams in the national economy, such as fundamental research in the field of relativistic nuclear physics and high-energy density physics in matter, problems of malignant tumor therapy, applied materials science problems, etc. Among the latter, tasks of research and control of electronic components under various types of radiation loads, particularly in charged particle fluxes with a wide spectrum of masses and energies, are becoming increasingly relevant. A synchrotron complex capable of simulating such conditions is becoming more and more in demand due to the intensive use of electronic equipment on spacecraft.

Pulsed laser generators allow concentrating radiation in a small volume and thereby obtaining record light brightness, which, when applied to plasma creation, makes it possible to achieve high radiation flux density on the target surface and plasma heating to temperatures that ensure the generation of charged particle beams with record ionization states and intensity. A characteristic feature of such a scheme is the ability to produce beams of short duration, for example, up to a few microseconds, which is required in a number of applications. Another technical advantage of laser sources, arising from the technological scheme, is associated with the possibility of quickly switching the generated beams from one type of ion to another from virtually the entire range of chemical elements. Such qualities of laser-plasma ion generators make them indispensable as part of accelerator injectors for comprehensive studies on the effects of ion beams on materials and various electronic components.

The use of CO_2-laser as an emitter gives the laser-plasma ion source additional advantages due to the technical simplicity of the CO_2-laser and low requirements for optical elements: the cost of the installation is relatively low even in the case of a frequency-operated laser with high (at least 100 J) output energy. Production facilities for housing a CO_2-laser are also characterized by relatively low requirements for cleanliness class, vibration resistance, thermal stabilization, etc. etc. in accordance with the simple laser technology and long radiation wavelength, which reduces both capital construction costs and operational expenses.

2. DESCRIPTION OF THE EXPERIMENTAL SETUP AND MEASUREMENT METHODOLOGY

The laser-plasma ion generator (LPIG) used in the described experiments consists of three main parts (Fig. 1): laser driver LD; vacuum target chamber TC and high-voltage extraction system ES.

Fig. 1. Schematic of laser-plasma ion generator:

As a laser driver, the FOCUS system was created, which is a deep modernization of the previously developed prototype of a pulsed-periodic CO_2-laser [1], aimed, firstly, at developing a fundamental laser-optical scheme and thereby increasing the peak radiation power of the device with unchanged laser pumping energy; secondly, at eliminating design deficiencies of the prototype device identified during operation, in order to increase the reliability and service life of the LPIG.

The basic physical scheme of radiation pulse formation in the FOCUS system is based on nonlinear optical effects during the propagation of CO_2-laser radiation in resonantly amplifying and absorbing media. This scheme was first proposed in [2] and was developed through numerical calculations and experiments using the idea of a multi-section design of the absorbing cell [3] to modify the front shape of the master oscillator (MO) pulse. The scheme uses cell AC1, consisting of three sections 30 cm long and filled with a mixture of $SF_6 + N_2$ according to the following law: section AC1-1 – total pressure 1000 mbar, SF_6 pressure 0.4 mbar; AC1-2 – 250 mbar, 0.8 mbar; AC1-3 – 62.5 mbar, 1.6 mbar. This method allows to specifically modify the radiation growth law after the MO [4], as a result of which the pulse is effectively shortened in duration during amplification.

The schematic of the FOCUS laser driver (LD) as a component of the LPIG is shown in Fig. 1. The radiation pulse of a single-mode single-frequency master oscillator *1,* which is described in detail in work [5], operating on the P(20) line of the 10 μm generation band, is modified in a three-section resonant absorption cell AC1 *2*, then using a flat diffraction grating *3* it is directed to a spatial filter (SF), which is a diaphragm *6* with an aperture located at the focus of a confocal pair of spherical mirrors *4*, *5* (the base of the telescopic pair $B = (R_1 + R_2)/2$, where R_1, R_2 are the radii of curvature of the long-focus and short-focus mirrors) and forms the beam distribution, cutting off high-order spatial harmonics so that the output beam becomes close to Gaussian. Another function of the telescopic pair is to increase the beam diameter for optimal amplification conditions (in this scheme, an increase of $M = R_1/R_2 = 3$ is established).

Further, the diffractively diverging laser beam, using a system of flat mirrors, makes the first pass through the amplifying medium *7*, then a pass through the absorption cell AC2 *8* with a length of 70 cm, filled with a mixture of $SF_6 + N_2$ up to a pressure of 150 mbar with SF_6 content at a pressure of 4 mbar. The second cell participates in the formation of the radiation rise front, and also serves as a decoupler for the multi-pass amplification scheme, preventing parasitic generation at the operating wavelength along the optical axis. After the second pass through the amplifier, the beam hits the convex mirror *9* of an off-axis (the angle of incidence on the small mirror is no more than 2°) Cassegrain telescope (the radii of curvature of the small and large mirrors are 1632 and 11000 mm, respectively) and, geometrically expanding, makes a third pass through the amplifier and falls on the focusing mirror *10*, after which the parallel beam with a diameter of 170 mm realizes the final fourth pass, maximally filling the active volume.

The active medium *7* of the amplifier module, detailed in [6], is created by pumping the vibrational-rotational levels of CO_2 molecules in a self-sustained discharge of the $CO_2/N_2/He = 1.5/1/7.5$ gas mixture at atmospheric pressure. The self-sustained volumetric discharge with X-ray beam preionization, converted from an electron gun, is formed between profiled electrodes in a gap with a cross-section of 17×17 cm^2 and a length of 125 cm. The discharge is powered in parallel by two eight-stage modules of the Arkadyev-Marx pulse voltage generator (PVG) with a voltage pulse amplitude of up to 400 kV at idle. The PVG systems and the working mixture circulation through the discharge volume ensure the laser operation with a repetition rate of up to 1 Hz.

The operational experience of the laser system prototype revealed some design flaws limiting continuous operation, which have been addressed in the current installation:

1) the PYa2 cell has been moved out of the laser volume to prevent breakdown of the optical windows' surface layer by laser radiation due to contamination in the working gas mixture flow and to reduce their radiation resistance;
2) the working part of the discharge electrodes' surface is made of 1 mm thick perforated stainless steel sheet with a honeycomb structure of holes for maximum electrode transparency (in the lower electrode for the passage of the preionizer X-ray beam, and in the upper one —to minimize laser radiation reflection from the electrode surface) instead of a brass mesh of comparable transparency, which completely eliminated electrode burnout from random local arc formations;
3) changes have been made to the PVG design of the amplifier module discharge power supply by replacing the 0.1 μF working capacitors with a working voltage of up to 50 kV with similar nominal elements rated at 100 kV, which increases the calculated PVG service life to 10^6 shots.

The output beam of the laser system with a diameter of $D = 170$ mm is directed by a system of flat mirrors through a vacuum optical window *11* into the TC, where a focusing scheme is located, consisting of a spherical mirror *12* with a relative aperture $F/D \approx 8.8$ and an auxiliary flat mirror *13.* The system allows concentrating the radiation of the laser beam on the surface of a cylindrical target at an angle of about 5° to the surface normal, which minimizes specular reflection from the target returning to the laser scheme, thereby reducing feedback between the target and the active medium. Such feedback can lead to parasitic generation in the amplification line and additional beam load on the optical elements of the laser. To obtain the most stable reproducible conditions for ion generation, the cylindrical target is rotated and displaced along the rotation axis by a small angle after each irradiation act, so that each subsequent radiation pulse hits a fresh area of the target.

The reflective elements used in the optical scheme are made of M0b copper, whose working surfaces, coated with gold, possess sufficiently high beam resistance. Transparent elements made of polycrystalline zinc selenide are anti-reflection coated for 10.6 µm. The focusing surfaces of optical elements have a spherical shape. Oblique beam incidence in the off-axis telescope of the amplification scheme and the focusing lens of the target chamber practically does not lead to aberrations due to the large radii of curvature of the mirrors.

The target chamber is shown in more detail in Fig. 2. Focusing the laser beam *1* on the target surface in the vacuum chamber *2* leads to the formation of plasma on the target surface and its subsequent heating by laser radiation to high temperatures and expansion into vacuum. The expansion occurs predominantly along the normal to the target surface, along which the axis of the time-of-flight tube *3* is located, where the plasma flow of the target material expands. At a drift distance determined by the requirements for the duration and current density of the ion beam, a high-voltage extraction system *4* (ES, *15* in Fig. 1), with which plasma charge separation occurs and an ion beam is formed *5* (*16* in Fig. 1).

Fig. 2. General view of the target chamber and extraction system:

In the described installation, a three-electrode system was used to form the ion beam, as shown in Fig. 3. The plasma jet *1*, passing a drift distance of 1935 mm from the target, reaches the first configured extraction electrode *2* with an axial opening of 15 mm in diameter, which is under a positive potential that can be adjusted in the range of (0-70) kV. The TC with vacuum equipment and target driver, which are installed on high-voltage insulators *6* (Fig. 2), are under the same potential. At a distance of 40 mm from the first one, the second electrode *3* of flat shape with an axial opening of 26 mm in diameter is placed under a negative potential, adjustable in the range of (0 ÷ –20) kV. The third flat ground electrode *4* with an axial opening diameter of 26 mm is placed with a gap of 7 mm from the second one, it completes the scheme of forming the ion beam profile.

Fig. 3. Three-electrode high-voltage extraction system:

The pulse shape at the output of the laser system is recorded in each shot using a digital oscilloscope Tektronix with a photon-drag (PD-30) type detector, installed in the beam reflected from the input window of the target chamber and focused into the 30 mm aperture of the PD-30 crystal.

The measured signal was calibrated according to the radiation power by preliminary measurement of the pulse energy with a Tektronix DPO 5104 thermocouple receiver. The time resolution of PD-30, as estimated from electrical characteristics, is not worse than 1 ns, the oscilloscope recording band is 1 GHz with a recording discreteness of 100 ps.

In Fig. Figure 4 shows the results of statistical processing of laser pulse data at the amplifier output during energy spectrum measurements: the average values of peak power (a), total energy (b), and full width at half maximum duration (c) were 6.25 ± 0.55 GW, 105.3 ± 6.3 J, 13.9 ± 1.7 ns with normal distribution approximation of the data. The data were obtained during two hours of operation of the FOCUS system with a pulse repetition rate of 1/16 Hz. This mode is determined by the conditions for measuring the ion expansion spectrum and is defined by the final pumping speed of the target chamber to restore the required vacuum level after target irradiation, as well as the speed of collecting the necessary amount of data per shot when measuring the energy spectrum of ion expansion.

Fig. 4. Statistical processing data of laser pulse characteristics at the output

A typical pulse shape in the radiation power scale is shown in Fig. 5. The pulse duration at half-maximum equals $\tau_{1/2} = (13.9 \pm 1.7)$ ns with a rise time $\tau_F \approx 4$ ns at the level (0.1-0.9). The latter characteristic is important for the generation of highly charged ions, as it determines the efficiency of plasma heating and achieving the maximum degree of ionization under conditions of comparable dynamics of the ion expansion process from the hot region. In the experiments described here, the laser output was limited in peak power to 1.5 GW at the entrance to the target chamber by diaphragming the beam with a through hole of 90 mm diameter.

Fig. 5. Typical pulse shape at the output of the FOCUS system.

Energy density distribution (1) and energy content in the beam (2) before the focusing lens of the target chamber ($F = 1500$ mm) (a) and in the focal plane (b), obtained by diffraction calculation of radiation propagation in the axial approximation using the program described in [1], are shown in Fig. 6. Here, the total energy $E_0 = 19$ J and the maximum beam energy density $e_0^1 = 0.96$ J/cm^2, and the maximum energy density in the spot focus $e_0^2 = 4.4 \cdot 10^4$ J/cm^2.

Fig. 6. Spatial profile (1, left scale) and energy content (2, right scale) of the laser beam

Let's estimate the effective flux density q_{AV}, at which the ion generation experiments described in the paper were conducted: taking the time interval and spatial boundary of the beam at 0.1 of the flux density level, then the averaged value $q_{AV} \approx 3.6\cdot 10^{11}$ W/cm^2, which corresponds to the time interval (−1, 32) ns on the pulse oscillogram and a spot diameter of 320 µm on the spatial form. Its effective value is apparently lower due to thermal conductivity into the peripheral heating area. Note that the frequently used estimate of flux density to characterize target irradiation conditions based on the maximum value at the pulse peak and the central part of the focal spot is $q_0 \approx 3\cdot 10^{12}$ W/cm^2, which is significantly higher than the averaged value.

To study the energy spectrum of ion scattering, a time-of-flight electrostatic cylindrical deflector with a rotation angle of 90° was used, as described in detail in [7], which was installed instead of the extraction system. The drift distance from the target to the detector, which was a vacuum electron multiplier (VEM) Electronic Tubes Ltd 143EM, was 3620 mm. Primary data from analyzer signals across the entire range of discrete analyzer tuning energies E ($E = GzU_0$, where $G = 20$ – geometric factor of the analyzer, z – ion charge, U_0 – voltage on the deflector plates) were recorded in real-time and processed using computer code, including identification of observed ion signals, their averaging over 10 measurements for each tuning point, interpolation, and obtaining the required characteristics of ions of individual charge states. Fig. 7 shows a typical oscillogram for bismuth ions obtained at a tuning energy E [keV]= $4z$, where bismuth ions are most represented in amplitude. At the next stage of reconstructing ion flow characteristics under the same irradiation conditions, measurements of the total ion current behind the extraction system were made, after which the averaged values were used to normalize partial currents in absolute units. As a result, particle densities were calculated at a given drift distance and in a given time interval. Fig. 8 shows a typical oscillogram of the total bismuth ion current in a series of 25 measurements, obtained with potentials on the first and second extraction electrodes of +62 kV and –5 kV respectively; the scatter is shown taking into account the standard deviations of the experimental data.

Fig. 7. Signals from the Bi ion analyzer at a tuning energy E [keV]= $4z$,

Fig. 8. Averaged form of the total bismuth ion current density (curve 2) and standard deviations (curves 1 and 3).

Data in Fig. 7, 8 illustrate the characteristic features of ion generation in laser plasma: a) the ion spectrum contains at least two groups of ions, high-energy and low-energy [8] (see Fig. 8a), which reflect the temporal behavior of the laser intensity and the spatial shape of the focal spot, with the maximum flux densities corresponding to the peak intensity of the laser pulse and the central regions of the focal spot, the fastest part of the ion beam is generated; b) as the average charge of the generated ions increases, their energy also increases (see Fig. 7), i.e. the high-energy "head" of the ion beam is formed predominantly by particles with high degrees of ionization.

3. CHARACTERISTICS OF Al, Fe AND Bi IONS AT THE OUTPUT OF THE LASER-PLASMA GENERATOR

Below are the practically interesting characteristics of Al, Fe, and Bi ions obtained under the irradiation and extraction conditions described above with a fixed laser flux density. This provides the simplest source configuration; when changing the element under study, the control is reduced only to adjusting the ion energy at the input to the RFQ linear accelerator, which according to preliminary calculations for the developed injector-linear accelerator is 9 keV/nucleon and consists of the initial ion expansion energy and the energy acquired during acceleration in the extraction system. Another cardinal parameter of the RFQ linear accelerator is the ratio of the energy of the accelerated ions to their charge which is expected to be adjustable in the range of 4-8 keV/charge, determining the selection of ion types from the source: for bismuth ions with a charge higher than 26, iron in the range of 7-14, aluminum in the range of 4-7.

In Fig. 9 shows the form of the reconstructed energy spectrum of bismuth ions with charge states that are candidates for acceleration in the developed injector, the dots show a discrete series of analyzer tuning energies during measurements. As can be seen, the energy spread of the main mass of ions is in the range of (70-250) keV, the average energy of ions from the series Bi^{27+} - Bi^{30+} is estimated as 155, 177, 189 and 200 keV respectively. Thus, for example, when using a Bi^{27+} ion in the injector, it is necessary to apply an accelerating voltage of 63.9 kV on the first extraction electrode. The same data in Fig. 9 are presented as the density of partial currents, which for the ions listed above are estimated by peak amplitudes as 0.5, 0.4, 0.3 and 0.15 mA/cm ^{2} respectively. The calculation of particle density in the time interval of 5 μs gives the values shown in Fig. 10 .

Fig. 9. Energy spectrum of bismuth ions: 1(○) - Bi^{27+}, 2(Δ) - Bi^{28+}, 3(◊) - Bi^{29+}, 4(☆) - Bi^{30+}.

Fig. 10. Partial currents of bismuth ions obtained after the extraction system: 1(○) - Bi^{27+}, 2(Δ) - Bi^{28+}, 3(◊) - Bi^{29+}, 4(☆) - Bi^{30+}.

Similar data are shown in Fig. 11-13 for Fe $^{10+}$, Fe $^{11+}$, Fe $^{12+}$ and Fe $^{14+}$ ions and in Fig. 14-16 for Al $^{4+}$, Al $^{5+}$, Al $^{6+}$ and Al $^{7+}$ ions. The average energy in the observed range was for iron ions respectively 15, 10, 7.5 and 5 keV, and for aluminum ions respectively 2.2, 1.8, 1.8 and 1.21 keV. The amplitudes of the partial current densities are estimated as 0.4, 0.8, 2.1 and 9.1 mA/cm ^{2} for iron ions and 0.7, 0.8, 1.0 and 1.21 mA/cm ^{2} for aluminum ions respectively. Particle densities are shown in Fig. 14, 17 respectively.

Fig. 11. Bismuth ion number density in the interval of 5 μs.

Fig. 12. Energy spectrum of iron ions: 1(○) – Fe $^{14+}$, 2(Δ) – Fe $^{12+}$, 3(◊) – Fe $^{11+}$, 4(☆) – Fe $^{10+}$.

Fig. 13. Partial currents of iron ions obtained behind the extraction system: 1(○) – Fe $^{14+}$, 2(Δ) – Fe $^{12+}$, 3(◊) – Fe $^{11+}$, 4(☆) – Fe $^{10+}$.

Fig. 14. Number density of iron ions Fe $^{10+}$ –Fe $^{14+}$ in the interval of 5 μs.

Fig. 15. Energy spectrum of aluminum ions: 1(○) – Al $^{7+}$, 2(Δ) – Al $^{6+}$, 3(◊) – Al $^{5+}$, 4(☆) – Al $^{4+}$.

Fig. 16. Partial currents of aluminum ions obtained behind the extraction system: 1(○) – Al $^{7+}$, 2(Δ) – Al $^{6+}$, 3(◊) – Al $^{5+}$, 4(☆) – Al $^{4+}$.

Fig. 17. Number density of aluminum ions Al $^{4+}$–Al $^{7+}$ in the interval of 5 μs.

The estimated particle density over the extraction length in the time interval of 5 μs for Bi $^{27+}$ ions is $2.8\cdot10^{8}$ cm $^{-2}$, for Fe $^{14+}$ ions – $1.4\cdot10^{10}$ cm $^{-2}$, for Al $^{7+}$ ions – $7.6\cdot10^{9}$ cm $^{-2}$.

The obtained results on the characteristics of generated ions in the laser-plasma source of the Kurchatov Complex of Theoretical and Experimental Physics of the National Research Center "Kurchatov Institute" (KCTEP NRC KI) allow calculating the necessary parameters of ions at the entrance to the RFQ linear accelerator of the particle injector under development. It differs from the configuration described in this paper by the drift length, which is reduced to 1650 mm. Such input parameters of bismuth, iron, and aluminum ions are given in Table 1, taking into account the reduction of the time interval for using the ion beam to 3 μs.

Table 1. Input parameters of Bi, Fe and Al ions under conditions of reducing the time interval of ion beam use to 3 μs

Ion type	Average energy, keV/nucleon	Extraction voltage, kV	Particle density, 10^{9} cm $^{-2}$
Bi $^{30+}$	0.957	56	0.04
Bi $^{29+}$	0.904	58.3	0.12
Bi $^{28+}$	0.847	60.9	0.18
Bi $^{27+}$	0.742	63.9	0.27
Fe $^{14+}$	0.268	35.1	13.4
Fe $^{12+}$	0.179	41.4	4.0
Fe $^{11+}$	0.134	45.3	2.0
Fe $^{10+}$	0.089	50.1	1.2
Al $^{7+}$	0.081	34.6	7.3
Al $^{6+}$	0.067	40.4	4.8
Al $^{5+}$	0.070	48.4	4.2
Al $^{4+}$	0.044	60.7	5.3

The obtained data allow for more detailed calculations of the linear accelerator-injector structure.

4. CONCLUSION

The paper describes the design and parameters of an ion source intended for particle injector from a wide range of elements of various masses. An important feature of the injector according to technical requirements is the operational flexibility in switching between types of generated ions from the entire range of elements from light to heavy. As an example from this range of elements, targets made of aluminum, iron, and bismuth were tested, which were irradiated with a constant laser radiation flux on the target, the level of which was selected based on the criterion of achieving sufficient ionization of the heaviest element ions, which in our experiments was bismuth. It was found that at a laser power level of approximately 1.5 GW and focusing the radiation on the target with a long-focus lens with a parameter $F/D \approx 8$, a plasma ionization level is achieved with a sufficiently high content of Bi $^{27+}$ ion, suitable for further acceleration in the injector. To simplify the technology of generating ions of lower mass, the achieved laser power level remained unchanged, which maximally simplified the process of switching from one element to another. In this mode, to change the type of generated ion, only a target change and extraction voltage adjustment were required to establish the optimal ion beam energy at the input to the RFQ linear accelerator.

The measurements showed that the tested irradiation and ion generation technology is quite effective in terms of generating light ions, despite the fact that at high radiation densities on the target, the total number of ions with the required charge state for acceleration decreases. The fact is that one of the requirements for the ion beam from the source is its fixed duration of a sufficiently small value. While maintaining a high irradiation flux density, the duration of light ion beams remains minimal, which, when converted to the number of particles in a beam of the required duration, leads to sufficiently high indicators that meet the requirements for the accelerator scheme. This is indicated by the numbers of iron and aluminum ions obtained in the described test experiments.

In general, it is shown that the demonstrated technological scheme of the laser-plasma ion source meets the requirements formulated for the developed particle injector into the synchrotron.

FUNDING

The work was carried out within the framework of the thematic plan of KKTEF NRC KI.

REFERENCES

1. *Satov Yu., Sharkov B., Haseroth H., Smakovskiy Yu, Makarov K., Kondrashev S., Roerich V., Stepanov A., Kugler H., Scrivens R., Camut O., Shumshurov A., Balabaev A., Charushin A.* // J. Russ. Laser Res. 2004. V. 25. № 3. P. 205. https://doi.org/10.1023/b:jorr.0000026779.64230.19
2. *Makarov K.N., Malyuta D.D., Nishchuk S.G., Rerikh V.K., Satov Yu.A., Smakovskiy Yu. B., Stepanov A.E., Khomenko S.V.*/ QE. 2001. V. 31. № 1. P. 23. https://doi.org/10.1070/QE2001v031n01ABEH001885
3. *Satov Yu.A., Smakovskiy Yu.B.* RF Patent 2 653 568, 2018.
4. *Satov Yu.A., Khrisanov I.A., Shumshurov A.V., Balabaev A.N., Losev A.A.* ITEP Preprint № 1–16, Moscow, 2016.
5. *Satov Yu.A., Sharkov B.Yu., Alekseev N.N., Shumshurov A.V., Balabaev A.N., Savin S.M., Belokurov A.D., Khrisanov I.A., Makarov K.N.* // PTE. 2012. № 3. P. 107. http://dx.doi.org/10.1134/S0020441212020108

6. *Satov Yu., Sharkov B., Smakovski Yu., Makarov K., Stepanov A., Roerich V., Kondrashev S., Shumshurov A., Balabaev A.* // J. Russ. Laser Res. 2004. V. 2. № 6. P. 524. http://dx.doi.org/10.1023/B:JORR.0000049085.71399.ed
7. *Satov Yu.A., Shumshurov A.V., Vasiliev A.A., Balabaev A.N., Losev A.A., Khrisanov I.A., Makarov K.N., Rerikh V.K.*/ 4. P. 108. http://dx.doi.org/10.1134/S0020441217030241
8. *Stepanov A.E., Satov Yu.A., Makarov K.N., Roerich V.C., Smakovskiy Yu.B., Maluta D.D., Starostin A.N.* // Plasma Phys. Control. Fusion. 2003. V. 45. № 7. P. 1261. https://doi.org/10.1088/0741-3335/45/7/315

FIGURE CAPTIONS

Fig. 1. Schematic of the laser-plasma ion generator: LD - laser driver - FOCUS system, TC - target chamber, ES - extraction system, *1* - single-mode single-frequency MO, *2* - three-section absorption cell AC1, *3* - diffraction grating, *4* - short-focus mirror SF, *5* - long-focus mirror SF, *6* - spatial filter, *7* - active medium of wide-aperture multi-pass amplification module, *8* - single-section absorption cell AC2, *9* - convex mirror of off-axis confocal telescope, *10* - focusing mirror of telescope, *11* - input window of vacuum target chamber, *12* - focusing lens, *13* - flat turning mirror, *14* - cylindrical target, *15* - high-voltage extraction system, *16* - output ion beam.

Fig. 2. General view of the target chamber and extraction system: *1* - laser beam, *2* - vacuum target chamber, *3* - drift tube, *4* - high-voltage extraction system, *5* - ion beam, *6* - high-voltage insulators. The wavy line shows the path of the laser beam, the dashed line - plasma jet of target material, solid line - ion beam path.

Fig. 3. Three-electrode high-voltage extraction system: *1* - plasma flow, *2* - first electrode with positive potential, *3* - middle electrode with negative potential, *4* - third grounded electrode.

Fig. 4. Statistical processing data of laser pulse characteristics at the output of the FOCUS system for a 2 hour test with a repetition rate of 1/16 Hz: **a** - peak pulse power, **b** - total energy, **c** - full width at half maximum.

Fig. 5. Typical pulse shape at the output of the FOCUS system.

Fig. 6. Spatial profile (1, left scale) and energy content (2, right scale) of the laser beam before the target chamber (**a**) and in the focal plane (**b**), where $E_0 = 19$ J - total beam energy, $e_0^1 = 0.96$ J/cm^2 - maximum beam energy density, $e_0^2 = 4.4 \cdot 10^4$ J/cm^2 - maximum energy density in the focal spot.

Fig. 7. Signals from the Bi ion analyzer at tuning energy E [keV] = $4z$, where the SEM signal amplitudes were maximum. Zero value on the time scale - the moment of target irradiation start, drift length 3620 mm.

Fig. 8. Averaged shape of the bismuth ion total current density (curve 2) and standard deviations (curves 1 and 3). Drift length 1935 mm: **a** - overview scale, **b** - arrival interval of high-energy ions.

Fig. 9. Energy spectrum of bismuth ions: 1(○) - Bi^{27+}, 2(Δ) - Bi^{28+}, 3(◊) - Bi^{29+}, 4(☆) - Bi^{30+}.

Fig. 10. Partial currents of bismuth ions obtained behind the extraction system: 1(○) - Bi^{27+}, 2(Δ) - Bi^{28+}, 3(◊) - Bi^{29+}, 4(☆) - Bi^{30+}.

Fig. 11. Bismuth ion number density in a 5 μs interval.

Fig. 12. Energy spectrum of iron ions: 1(○) - Fe $^{14+}$, 2(Δ) - Fe $^{12+}$, 3(◊) - Fe $^{11+}$, 4(☆) - Fe $^{10+}$.

Fig. 13. Partial currents of iron ions obtained behind the extraction system: 1(○) - Fe $^{14+}$, 2(Δ) - Fe $^{12+}$, 3(◊) - Fe $^{11+}$, 4(☆) - Fe $^{10+}$.

Fig. 14. Density of iron ions Fe $^{10+}$ ÷Fe $^{14+}$ in the interval of 5 μs.

Fig. 15. Energy spectrum of aluminum ions: 1(○) – Al $^{7+}$, 2(Δ) – Al $^{6+}$, 3(◊) – Al $^{5+}$, 4(☆) – Al $^{4+}$.

Fig. 16. Partial currents of aluminum ions obtained behind the extraction system: 1(○) – Al $^{7+}$, 2(Δ) – Al $^{6+}$, 3(◊) – Al $^{5+}$, 4(☆) – Al $^{4+}$.

Fig. 17. Density of aluminum ions Al $^{4+}$–Al $^{7+}$ in the interval of 5 μs.

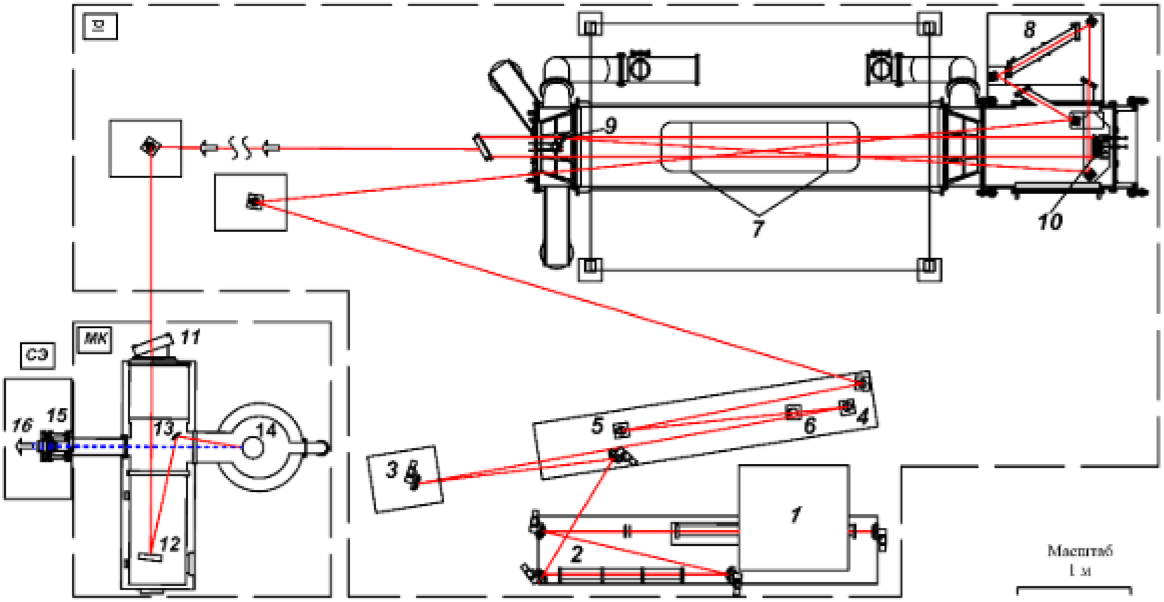

Fig. 1.

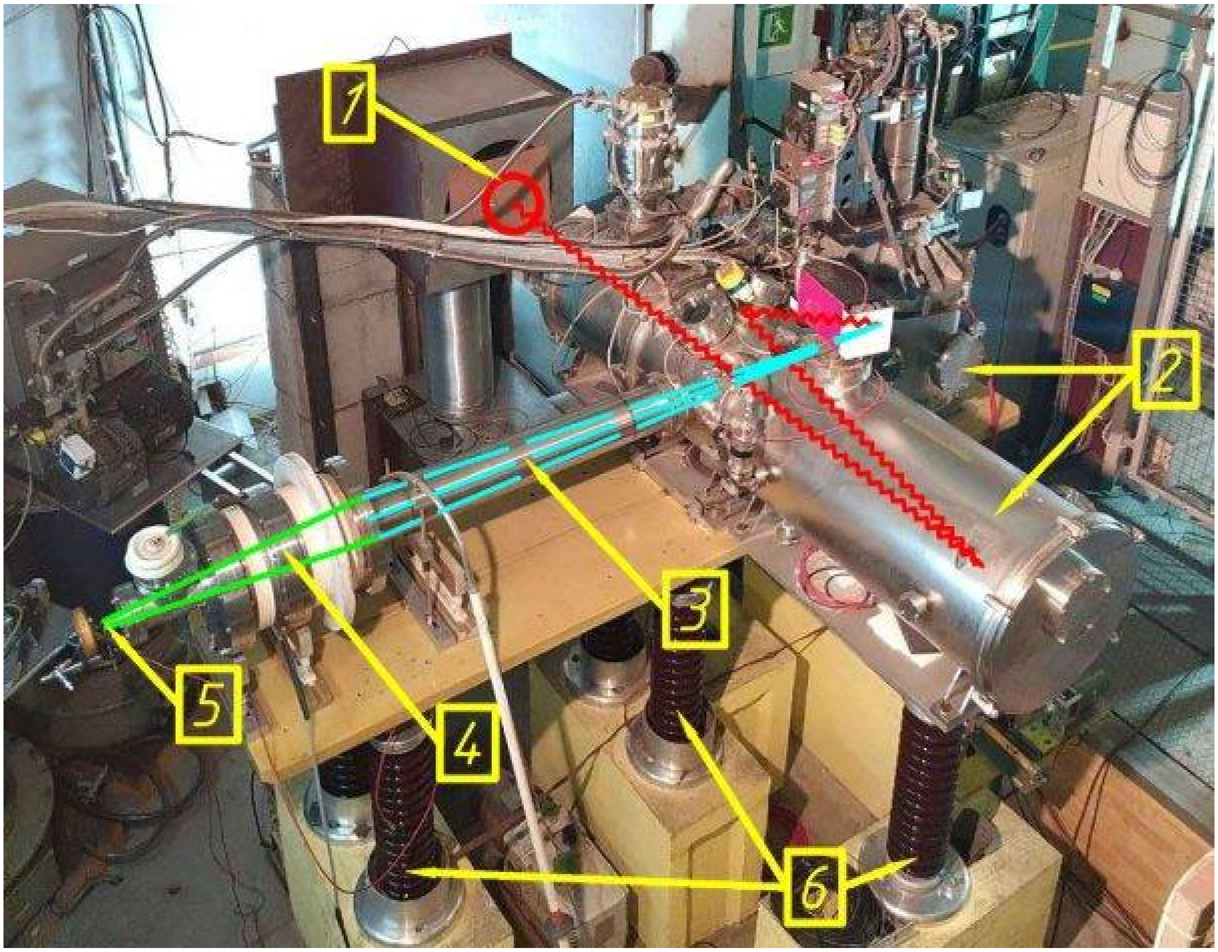

Fig. 2.

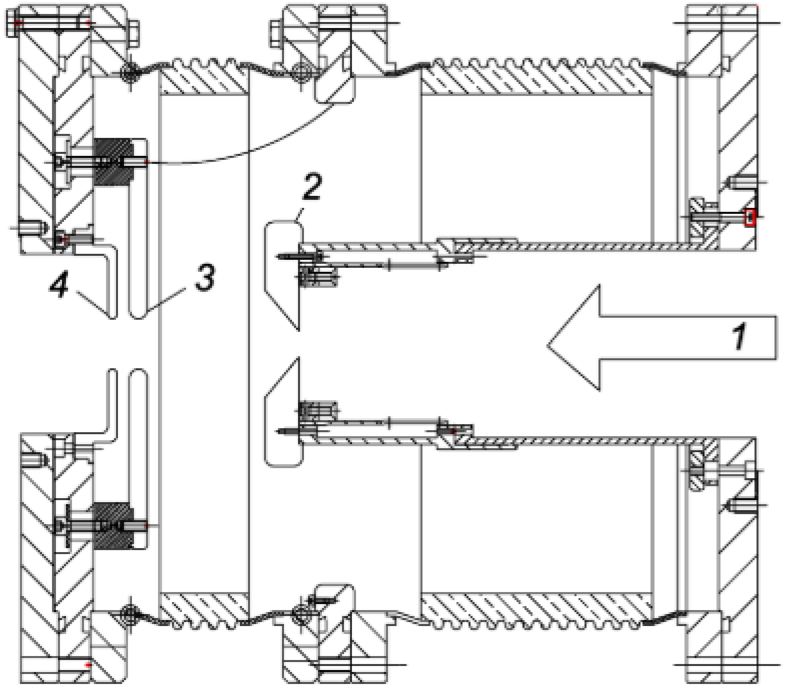

Fig. 3

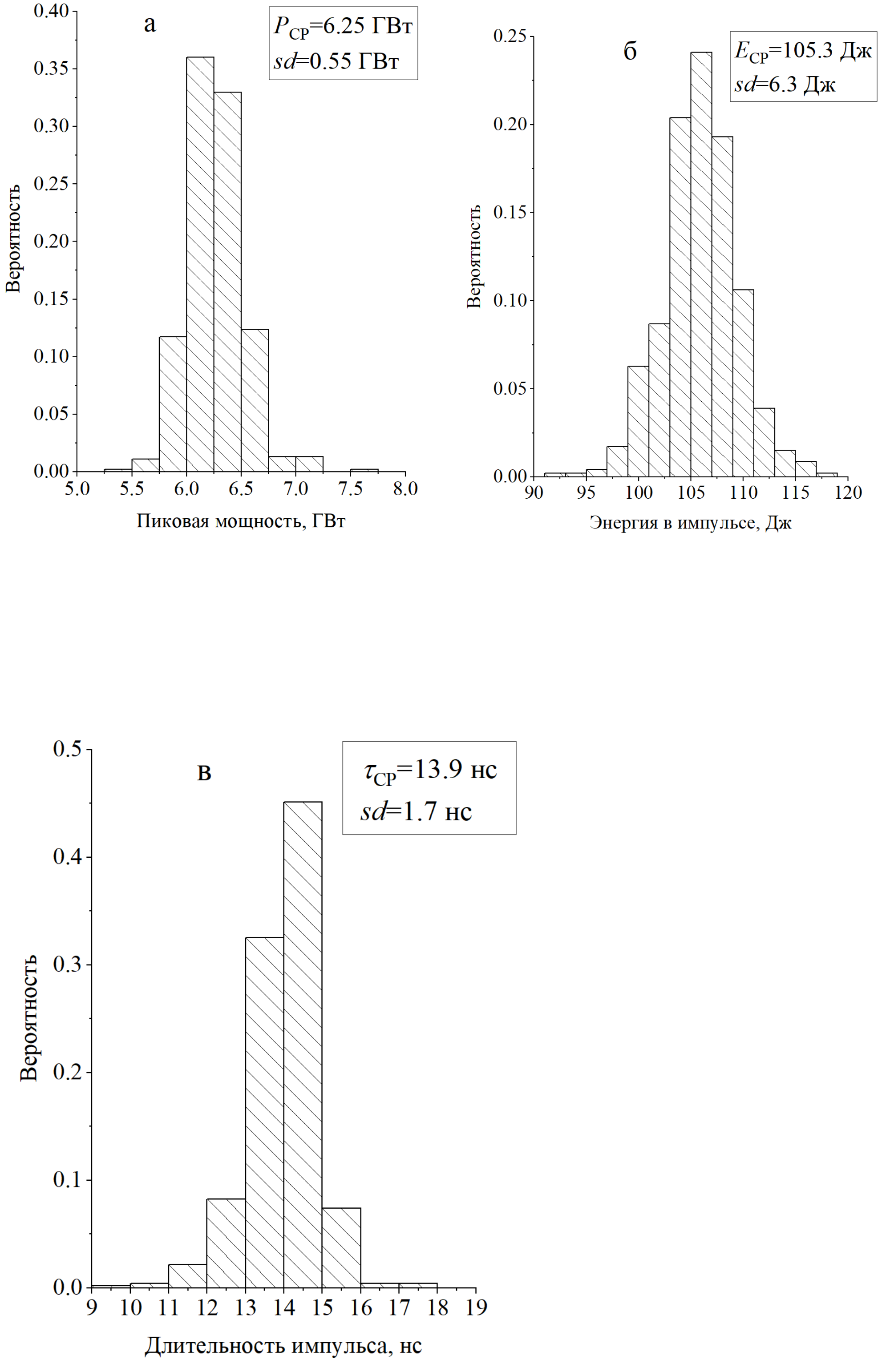
а
P_{CP}=6.25 ГВт
sd=0.55 ГВт
Вероятность
0.00
0.05
0.10
0.15
0.20
0.25
0.30
0.35
0.40
5.0
5.5
6.0
6.5
7.0
7.5
8.0
Пиковая мощность, ГВт
б
E_{CP}=105.3 Дж
sd=6.3 Дж
Вероятность
0.00
0.05
0.10
0.15
0.20
0.25
90
95
100
105
110
115
120
Энергия в импульсе, Дж
в
τ_{CP}=13.9 нс
sd=1.7 нс
Вероятность
0.0
0.1
0.2
0.3
0.4
0.5
9
10
11
12
13
14
15
16
17
18
19
Длительность импульса, нс

Fig. 4.

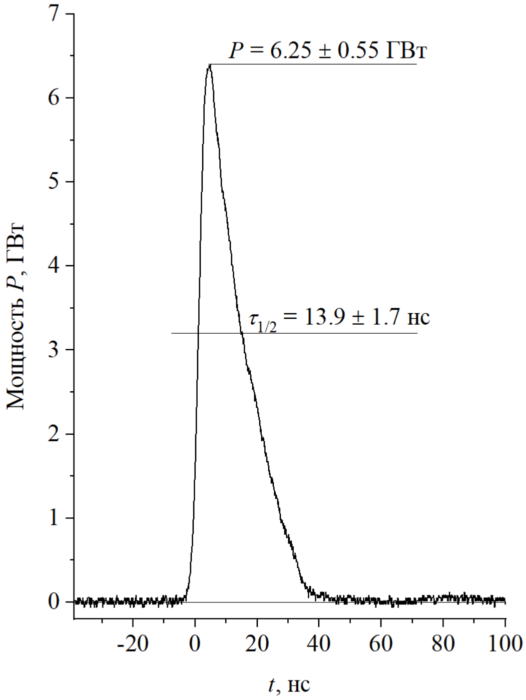

$P = 6.25 \pm 0.55$ ГВт
$\tau_{1/2} = 13.9 \pm 1.7$ нс
Мощность P, ГВт
t, нс
0
1
2
3
4
5
6
7
-20
0
20
40
60
80
100

Fig. 5.

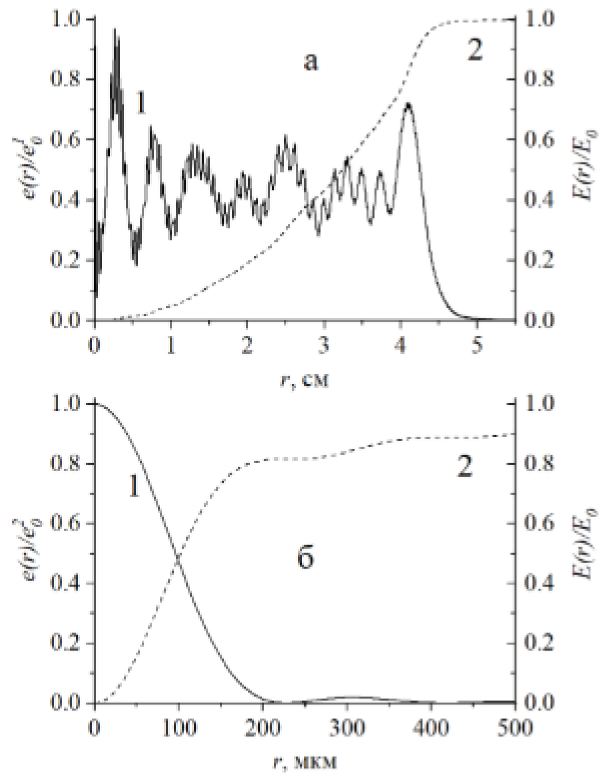
а
1
2
e(r)/e_0^1
E(r)/E_0
r, см
0.0
0.2
0.4
0.6
0.8
1.0
0
1
2
3
4
5
б
1
2
e(r)/e_0^2
E(r)/E_0
r, мкм
0
100
200
300
400
500

Fig. 6.

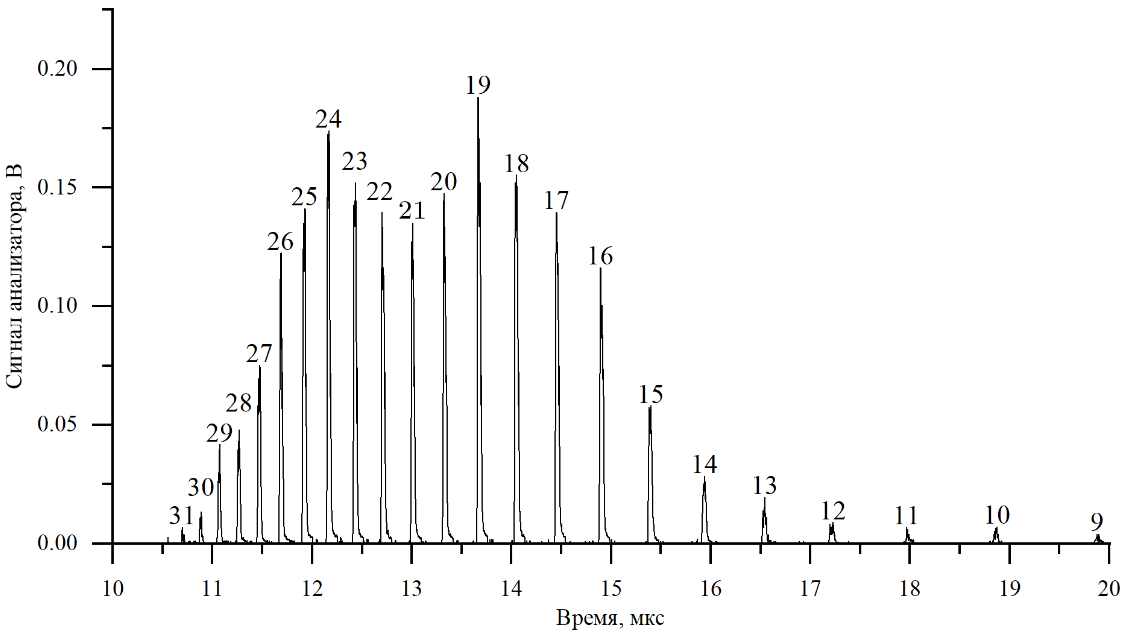
Сигнал анализатора, В
0.00
0.05
0.10
0.15
0.20
Время, мкс
10
11
12
13
14
15
16
17
18
19
20
31
30
29
28
27
26
25
24
23
22
21
20
19
18
17
16
15
14
13
12
11
10
9

Fig. 7.

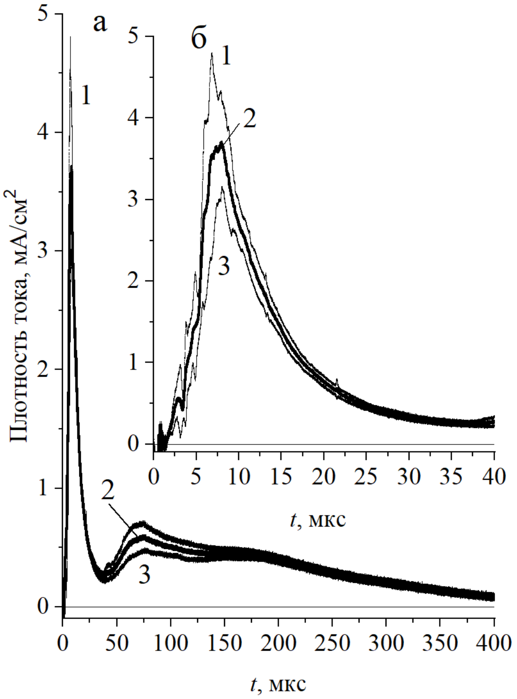
а
б
1
2
3
Плотность тока, мА/см^2
t, мкс
0
1
2
3
4
5
0
50
100
150
200
250
300
350
400
0
5
10
15
20
25
30
35
40

Fig. 8.

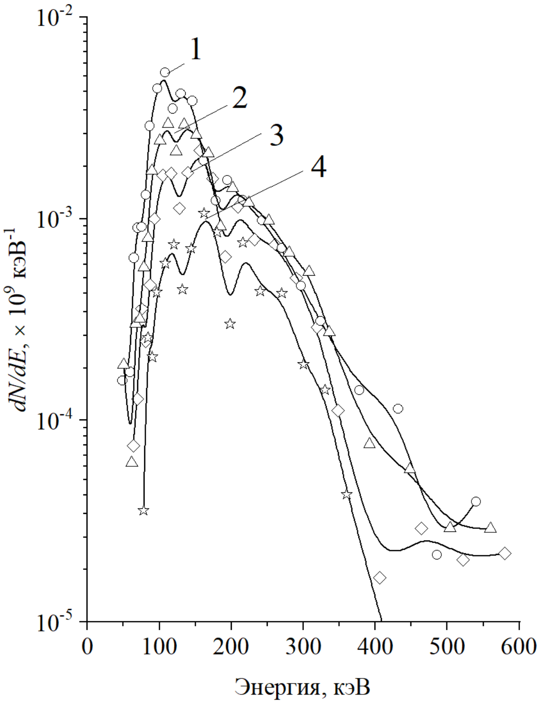
10^{-2}
10^{-3}
10^{-4}
10^{-5}
dN/dE, × 10^9 кэВ$^{-1}$
1
2
3
4
0
100
200
300
400
500
600
Энергия, кэВ

Fig. 9.

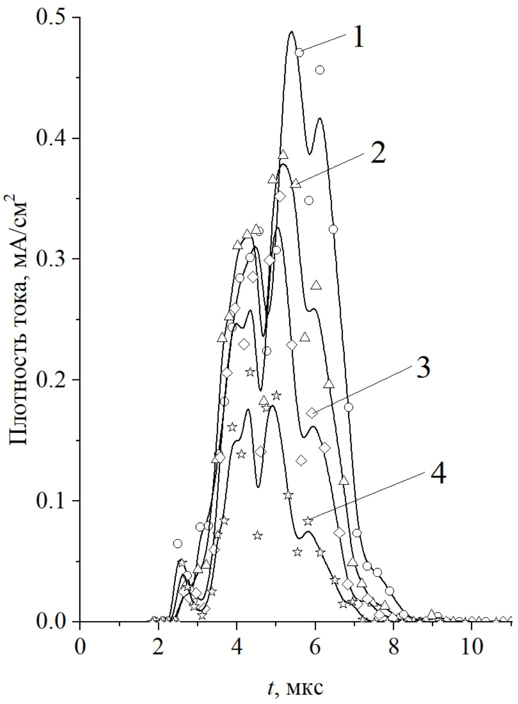

Fig. 10.

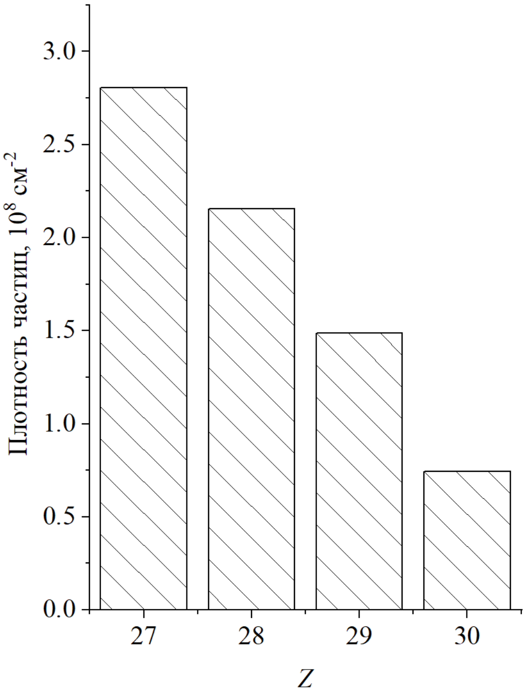

Fig. 11.

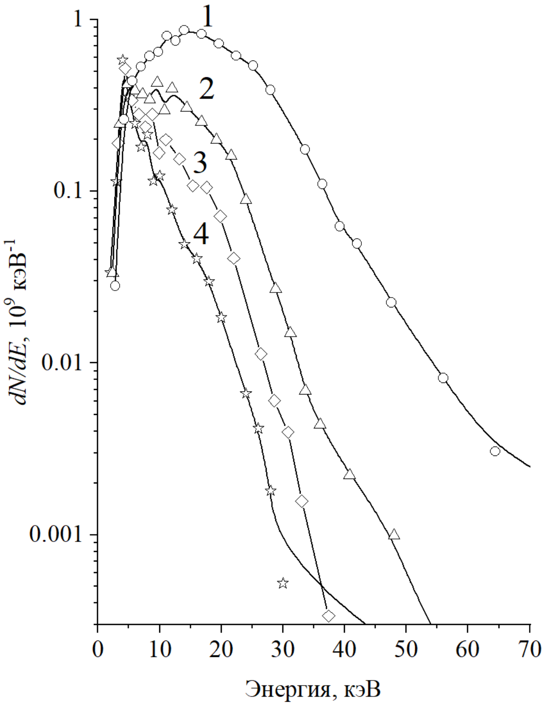

1
2
3
4
1
0.1
0.01
0.001
dN/dE, 10^9 кэВ$^{-1}$
0
10
20
30
40
50
60
70
Энергия, кэВ

Fig. 12.

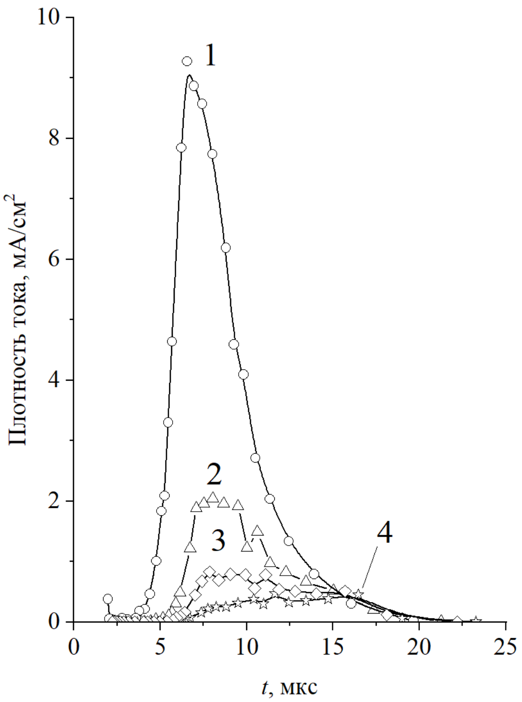

Fig. 13.

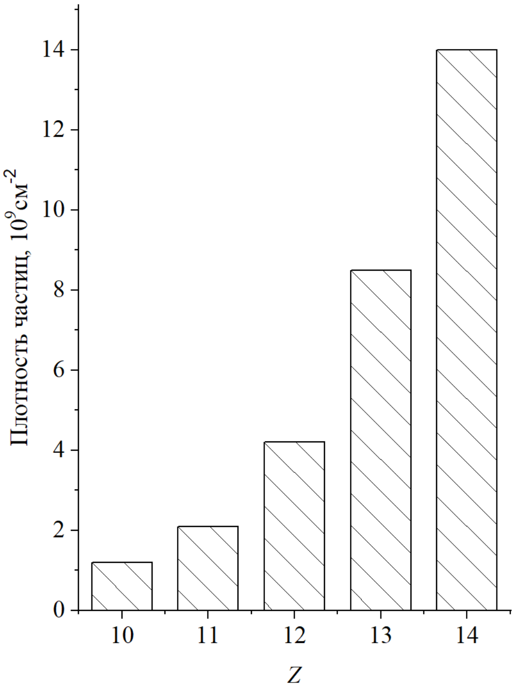

Fig. 14.

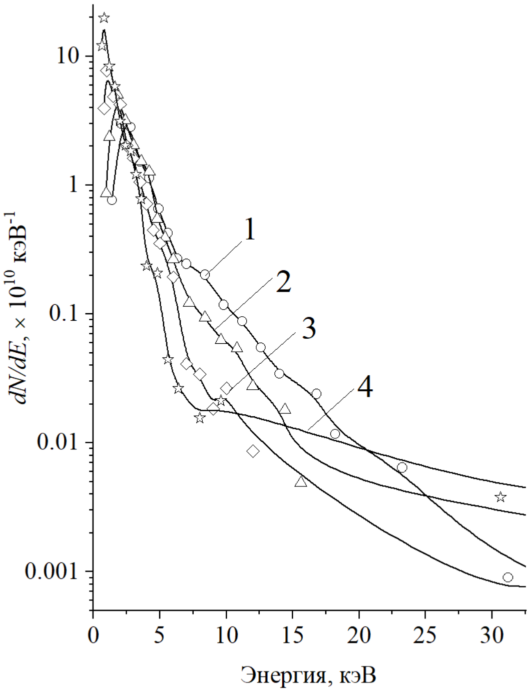

dN/dE, × 10^10 кэВ^-1
10
1
0.1
0.01
0.001
0
5
10
15
20
25
30
Энергия, кэВ
1
2
3
4

Fig. 15.

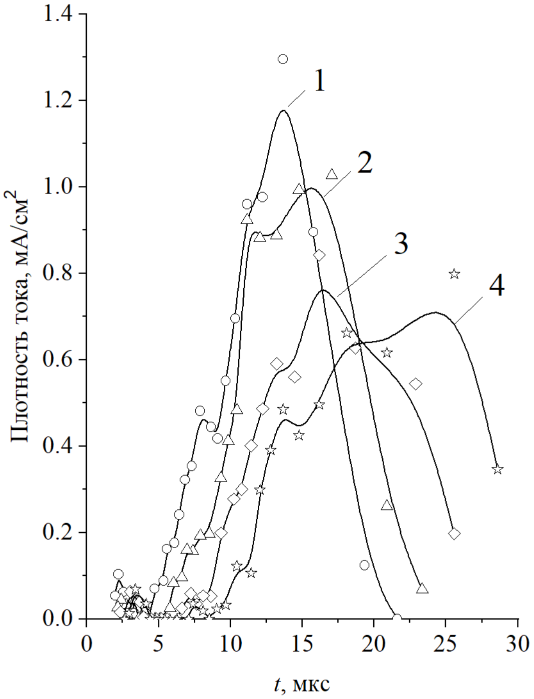

1.4
1.2
1.0
0.8
0.6
0.4
0.2
0.0
Плотность тока, мА/см^2
0
5
10
15
20
25
30
t, мкс
1
2
3
4

Fig. 16.

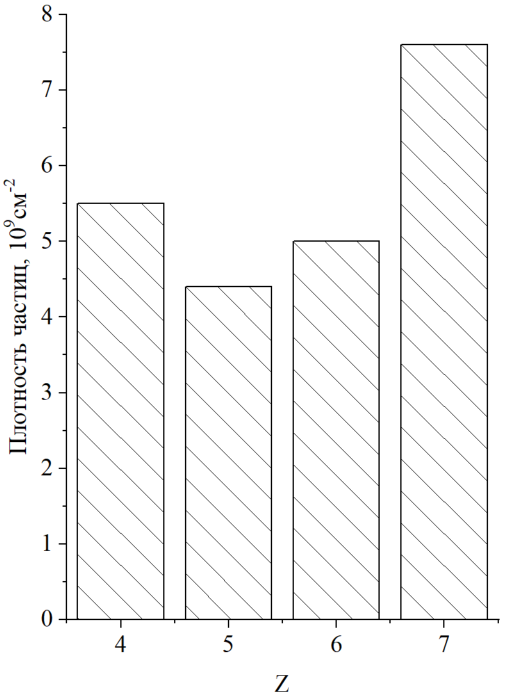

Fig. 17.